SAND--88-1403C

DE88 012336

SAND88-1403C

Analysis of the Late Core Melt Progression Phase of Severe Reactor Accidents Using the MELPROG Code*

S.S. Dosanjh

Reactor Safety Theoretical Physics Division
Sandia National Laboratories
Albuquerque, NM 87185

June 1988

This work will be submitted for presentation at the Severe Accident Thermal Hydraulics session of the 1988 ANS/ENS International Conference, which will be held in Washington, D.C., on October 30 - November 4, 1988.

* This work was supported by the United States Nuclear Regulatory Commission and was performed at Sandia National Laboratories, which is operated for the U.S. Department of Energy under contract number DE-AC04-76DP00789.

ABSTRACT

The two-dimensional (r-z) MELt PROGression (MELPROG) computer code is being developed to analyze severe light water reactor accidents from accident initiation through vessel failure. The MELPROG code is comprised of several explicitly linked modules that analyze different aspects of an accident. This paper describes the MELPROG models that are used to study the late core melt progression phase of severe accidents. Particular attention is given to the DEBRIS module that analyzes melt progression in particle beds that can form in the reactor core and the lower plenum during accidents like Three-Mile Island. Other modules in the MELPROG code are briefly described and results from a sample calculation are presented to demonstrate the capabilities of the code.

NOMENCLATURE

a_v	surface area of the debris per unit volume [m^2/m^3]
c_p	specific heat at constant pressure [J/kg•K]
d_p	particle diameter [mm]
D	mass diffusivity [m^2/s]
g	gravitational acceleration [m/s^2]
h	enthalpy [J/kg]
h_f	heat of fusion [J/kg]
H	heat transfer coefficient [W/m^2K]
k	thermal conductivity [W/m•K]
n	particle density [particles/m^3]
P_c	capillary pressure [N/m^2]
P_g	gas pressure [N/m^2]
P_l	liquid pressure [N/m^2]
q_c	energy released by oxidation [W/m^3]
Q	decay heat [W/kg of UO_2]
r	radial distance [m]
R_j	rate of production of species j by oxidation [kg/m^3s]
S	saturation or liquid fraction, $\alpha_l/(\alpha_l+\alpha_g)$
S_e	effective saturation, $S_e=(S-S_r)/(1-S_r)$
S_r	residual saturation
t	time [s]
T	temperature of the melt and solid debris [K]
T_g	temperature of the gas
u	liquid volumetric flux in the z direction [m/s]
U	velocity at which the solid collapses [m/s]
v	liquid volumetric flux in the r direction [m/s]
Y_{ij}	volume fraction of species j in phase i
z	distance from bottom [m]

Greek

α	volume fraction
Γ	rate of destruction of particles [particles/m^3s]
γ	surface tension [N/m]
ϵ	emissivity
θ	liquid-solid contact angle [°]
κ	permeability [m^2]
μ	viscosity [Pa•s]
ρ	theoretical density [kg/m^3]

Subscripts

g	gas
l	liquid
s	solid

1. INTRODUCTION

The two-dimensional (r-z) MELt PROGression (MELPROG) computer code [1] is being developed to analyze severe light water reactor accidents from accident initiation through vessel failure. The MELPROG code is comprised of several explicitly linked modules that analyze different aspects of an accident. At the beginning of an accident, the CORE module calculates heat transfer, oxidation, clad melting, dissolution and candling in the reactor core. If the fuel rods fragment, as happened at Three-Mile Island [2], core melt progression is analyzed in the DEBRIS module: this module is also used to model rubble beds that can form in the lower plenum. Heat transfer, oxidation, melting, dissolution, melt relocation and refreezing are all considered in the DEBRIS module.

Vapor and coolant flow in the core and through the vessel are treated in the FLUIDS module. This module also models the relocation of solid and molten materials from the reactor core into the lower plenum. Detailed heat transfer and structural mechanics calculations are performed in the STRUCTURES module for the vessel walls, various support plates, the core baffle, the core barrel, core support columns and other structures in the vessel. Three-dimensional, dynamic view factors are calculated in the RADIATION module that provides boundary conditions for the CORE, DEBRIS and STRUCTURES modules. Additional MELPROG modules are being developed to analyze fuel-coolant interactions, fission product release and the ejection of debris from the reactor vessel into the containment building.

This paper describes the MELPROG models that are used to study the late core melt progression phase of severe accidents. Particular attention is given to the DEBRIS module. Brief descriptions of the FLUIDS, STRUCTURES and RADIATION modules are provided in Sections 2.2, 2.3 and 2.4, respectively. Results from a sample calculation are presented to demonstrate the capabilities of the code and the effect of core melt progression on oxidation is addressed.

2. ANALYSIS

2.1 DEBRIS MODULE

A detailed description of the debris meltdown model and the solution technique is given in Ref. [3]. A discussion of the governing equations follows. Correlations are used to model drag forces, radiation heat transfer in the particle bed and chemical interactions. The effects of uncertainties in these correlations are discussed in Refs. [3-4].

Mass conservation equations for each species. A two-dimensional (r-z) momentum equation accounts for melt relocation due to both gravity and capillary forces; viscous drag is included by modifying Darcy's Law to account for undersaturated flow, and the wetting behaviour of molten stainless steel in contact with UO_2 is modeled using the formulation suggested by Scheidegger [5]. As solid melts in the center of the bed, the porosity increases; collapse of the bed is incorporated using a critical minimum solid volume fraction $\alpha_{s,min}$. The energy equation considers conduction and radiation heat transfer in the bed, and phase diagrams are used to model Fe-Zr and U-Zr-O interactions.

2.1.1 Conservation of Mass

Mass conservation equations are solved for each species j: j=1,2,3,4 and 5 corresponding to UO_2, ZrO_2, Zr, stainless steel and Ag-In-Cd. Balancing the mass stored in a differential control volume, convection by the liquid and the solid (as it collapses) and production (or depletion) gives

$$\frac{\partial}{\partial t}\left[\alpha_l Y_{lj}\rho_{lj}\right] + \bar{\nabla}\cdot\left[Y_{lj}\rho_{lj}\bar{u}\right] + \frac{\partial}{\partial z}\left[\alpha_s Y_{sj}\rho_{sj}U\right]$$

$$= -\frac{\partial}{\partial t}\left[\alpha_s Y_{sj}\rho_{sj}\right] + \dot{R}_j , \qquad (1)$$

where the subscripts l and s refer to liquid and solid, respectively, $\bar{u}=(u,v)$ is the liquid superficial velocity, U is the velocity at which the solid collapses, α is a volume fraction, Y_{ij} is the volume fraction of phase i that is occupied

by species j, and R_j is the rate of production of species j by oxidation.

Note that species diffusion is neglected in Eq.(1). Typical diffusivities for liquids near their melting points are on the order of 10^{-9} m^2/s [6]. For time scales on the order of 10^3 s, the distance characteristic of diffusion, $[Dt]^{1/2}$, is approximately 10^{-3} m. That is, liquid phase diffusion is only important over length scales comparable to the average particle diameter.

2.1.2 Liquid Motion

Balancing viscous drag (which is assumed to vary linearly with velocity), gravity and changes in pressure gives:

$$\rho_l \frac{\partial \bar{u}}{\partial t} + \frac{\mu}{\kappa_l} \bar{u} = - \bar{\nabla} P_l - \bar{g} \rho_l \quad , \tag{2}$$

where μ is the dynamic viscosity of the liquid, g is the gravitational acceleration and κ_l is the relative permeability. Capillary forces enter Eq.(2) through the term involving the liquid pressure, P_l. The capillary pressure is defined as the difference between P_l and the gas pressure, P_g (that is, $P_c=P_g-P_l$) [5]. Taking the gas flow to be isobaric gives $\nabla P_l=-\nabla P_c$. From Eq.(2) it is therefore evident that capillary forces move liquid into regions of high P_c.

In order to solve Eq. (2) the relative permeability κ_l and the capillary pressure P_c must be specified. In fully saturated flow, κ_l equals the permeability κ, while in undersaturated flow, only a fraction of the solid is in contact with liquid and κ_l is proportional to κ; the proportionality constant is a function of the saturation S, which is defined as the fraction of nonsolid volume occupied by liquid (i.e. $S=\alpha_l/(\alpha_l+\alpha_g)$). Reed [7] gives for κ_l:

$$\kappa_l = \begin{cases} \kappa S_e^3 & , \text{ for } S>S_r \\ 0 & , \text{ for } S \leq S_r \end{cases} \tag{3}$$

where $S_e=(S-S_r)/(1-S_r)$ and the residual saturation S_r is defined as the threshold value of saturation below which bulk liquid

motion ceases. For $S \leq S_r$, $\kappa_l = 0$ and Eq. (2) requires that $\bar{u} = 0$. When the saturation S is less than the residual saturation S_r, the liquid consists of unconnected pendular rings. Liquid starts to flow when S is increased to the point that these rings touch and coalesce [8]. When the liquid wets the solid ($0° < \theta < 90°$),

$$S_r = \frac{1}{86.3} \left[\frac{\gamma \cos\theta}{\kappa \rho_l g} \right]^{0.263} , \tag{4}$$

where γ is the surface tension and θ is the liquid-solid contact angle [9]. In a nonwetting system ($90° < \theta < 180°$), $S_r = 0.0$. The dependence of S_r on the porous matrix is contained in the permeability κ. Increasing the particle diameter or the porosity raises κ and leads to lower values of S_r. For packed beds consisting of small, tightly packed particles, the saturation must be increased to a high value before bulk liquid motion is observed. Bird [10] derives the following relation for κ by modeling the porous solid as a bundle of capillary tubes:

$$\kappa = \frac{d_p^2 \, \epsilon^3}{150 \, (1-\epsilon)^2} , \tag{5}$$

where the factor of 150 is determined empirically.

Leverett [8] derived the following equation for the capillary pressure P_c using dimensional analysis: $P_c = J \, \gamma \cos\theta \, (1-\alpha_s)^{1/2} / \kappa^{1/2}$, where J is a function of S_e only. Hoffman and Barleon [11] give an empirically determined relation for J: $J = a \, (S_e + b)^{-c}$, where a=0.38, b=0.014 and c=0.27. Therefore,

$$P_c = a \, (S_e + b)^{-c} \, \gamma \cos\theta \, \frac{\sqrt{150} \, \alpha_s}{d_p (1-\alpha_s)} . \tag{6}$$

Because P_c decreases as the particle diameter d_p increases, capillary forces are small in beds with large particles. For $0° < \theta < 90°$, increasing the solid fraction α_s or decreasing the saturation S_e increases P_c; capillary forces therefore move liquid into regions of high α_s (low porosity) and low saturation. For $90° < \theta < 180°$, decreasing α_s or increasing S_e increases P_c; capillary forces therefore move liquid into regions of low α_s

(high porosity) and high saturation. That is, melt tends to agglomerate in a nonwetting system. This effect has been observed in stainless steel-UO_2 beds in both the Molten Pool (MP) and Dry Capsule (DC) experiments [12-13].

2.1.3 Solid Motion

In order to determine the solid velocity U, the manner in which a high porosity bed collapses must be specified. It is assumed here that solid begins collapsing downward when the solid fraction falls below a critical value $\alpha_{s,min}$ and that $\alpha_s=\alpha_{s,min}$ in regions into which solid is collapsing.

The particle density n is determined from

$$\frac{\partial n}{\partial t} + \frac{\partial}{\partial z} nU = \Gamma \quad , \tag{7}$$

where Γ is the rate of destruction by phase changes. After solving Eq.(7) for n, the particle diameter is determined from $d_p=(6\alpha_s/n\pi)^{1/3}$.

2.1.4 Conservation of Energy

Balancing the energy stored in the solid and the liquid, convection by the liquid and the solid (as it collapses), diffusion and internal heat generation gives:

$$\frac{\partial}{\partial t} \sum_j \left[\alpha_s Y_{sj}\rho_{sj}h_{sj} + \alpha_l Y_{lj}\rho_{lj}h_{lj}\right] + \bar{\nabla}\cdot\left[\bar{u} \sum_j Y_{lj}\rho_{lj}h_{lj}\right]$$

$$+ \frac{\partial}{\partial z}\left[\alpha_s U \sum_j Y_{sj}\rho_{sj}h_{sj}\right] = \bar{\nabla}\cdot k_{eff}\bar{\nabla}T + \left[\alpha_s\rho_{s1}Y_{s1} + \alpha_l\rho_{l1}Y_{l1}\right]Q$$

$$+ q_c - a_v H\,(T-T_g) \quad , \tag{8}$$

where h_{ij} is the enthalpy of species j in phase i, k_{eff} is an effective thermal conductivity which accounts for both conductive and radiative heat transfer in the porous solid, Q is the decay heat expressed as energy release per mass of UO_2, q_c is the rate

at which energy is released by combustion, H is a heat transfer coefficient between the debris and the vapor, T_g is the vapor temperature and a_v is the surface area of the debris per unit volume. It is assumed here that the melt and the solid debris are in local thermal equilibrium (this is a reasonable assumption because melt velocities in the bed are low and the solid surface area per unit volume is large).

Radiation heat transfer in the packed bed is incorporated using a modified gas conductivity, $k_g^*=k_g+k_{rad}$, where $k_{rad}=4\epsilon\sigma d_p T^3$, ϵ is the emissivity of the solid and σ is the Stefan-Boltzmann constant [14]. Empirical correlations for k_{eff} in solid-gas systems are available in the literature [14]. However, in the current problem, three phases (solid, liquid and gas) are present. In calculating k_{eff}, the solid and the liquid are treated as a single component with a volume averaged thermal conductivity k_σ:

$$k_\sigma = \frac{1}{\alpha_s + \alpha_l}\left[\alpha_s \sum_j Y_{sj}k_{sj} + \alpha_l \sum_j Y_{lj}k_{lj}\right] \quad . \tag{9}$$

For a single phase i, k_σ depends only on Y_{ij} and k_{ij}. The following correlation gives k_{eff} [14]:

$$k_{eff} = \psi\, k_g^* + \frac{1-\psi}{k_\sigma\omega + k_g^*(1-\omega)}\, k_\sigma k_g^* \quad , \tag{10}$$

where $\omega=0.3\alpha_g^{1.6}(k_s/k_g^*)^{-0.044}$, $\psi=(\alpha_g-\omega)/(1-\omega)$ and α_g is the volume fraction occupied by gas. In the limit of a gas volume fraction of zero, both ω and ψ approach zero and consequently, $k_{eff}=k_\sigma$. On the other hand, in the limit of a gas volume fraction of one, ψ approaches one and $k_{eff}=k_g^*$.

2.1.5 Chemical Interactions

When the temperature surpasses 2100 K, molten Zr dissolves both UO_2 and ZrO_2 [15,16]. In this study these dissolution processes are taken to be symmetric with respect to UO_2 and ZrO_2 compositions. The solubilities of UO_2 and ZrO_2 in molten Zr are computed from the U-Zr-O liquidus temperature. Although Zr-UO_2, Zr-ZrO_2 and ZrO_2-UO_2 pseudo binary phase diagrams are available in the literature [15,16], a ternary U-Zr-O phase diagram is not currently available. Ternary liquidus temperatures are

determined in this study following the interpolation method suggested in Ref. [17]:

$$T_L = \frac{\sum_{\substack{i,j \\ i\neq j}} f_i f_j T_{Lij}}{\sum_{\substack{i,j \\ i\neq j}} f_i f_j} \quad , \tag{11}$$

where the f's are atomic fractions and T_{Lij} is the liquidus temperature for the i-j binary phase diagram. Equation (11) correctly reduces to $T_L=T_{Lij}$ when only two components are present.

2.1.6 Closure

In order to complete the preceding set of equations, oxidation rates, properties and initial conditions must be specified. Zirconium oxidation is modeled by the reaction $Zr+2H_2O \rightarrow ZrO_2+2H_2$ and the kinetics data given by Prater and Courtright [18] are utilized. Properties given by Hagrman et al. [15,16] are currently used. Initial conditions are discussed further in the next section.

2.2 FLUIDS MODULE

Compressible flow equations are solved for four fields: vapor, coolant, solid debris and melt. Typically, the last two fields, solid debris and melt, are only operational for short periods of time. For example, when debris is released from the reactor core or when a structure fails, the FLUIDS module calculates the motion of the debris until it reaches a pre-existing bed or lands on a plate. (From this point in time onward, this debris is analyzed in the DEBRIS module.)

Coupled mass, momentum and energy equations are solved for each field. An additional mass conservation equation is solved for hydrogen. Heat transfer and drag coefficients are used to model energy transfer and drag forces between the various fields, respectively. These coefficients are determined using a number of flow regime maps.

The governing equations are solved using the semi-implicit, two-step SETS method [19]. A fairly coarse grid is used for the fluids calculation, whereas the other modules use a much finer grid. In the demonstration calculation discussed in Section 3, 70 computational cells are used in the FLUIDS module while the DEBRIS module uses 750 cells.

2.3 STRUCTURES MODULE

In every fluids computational cell, a one-dimensional heat transfer calculation is performed for each structure. Axial conduction is considered for plates whereas walls are analyzed in the radial direction. The analysis considers both ablation and bulk melting. Mechanical failure is included using a correlational approach. For instance, the Larson-Miller Parameter correlation [20] is used to model plastic behavior and high temperature creep.

2.4 RADIATION MODULE

The RADIATION module determines boundary conditions for the STRUCTURES and DEBRIS modules. This module also provides volumetric energy sources to the FLUIDS module to account for absorption by water and steam. All surfaces are modeled as diffuse emitters, absorbers and reflectors, with constant emissivities. Three-dimensional view factors are calculated using a combination of a net enclosure model and a flux model. A temperature and pressure dependent mass absorptance is used for steam whereas a constant value is specified for water. Hydrogen is assumed to be transparent.

3. RESULTS

A demonstration calculation was conducted to illustrate the capabilities of the models discussed in the preceding section. Shown in Fig. 1 is a schematic of the reactor vessel model used in this calculation; this model is based on the design of a Surry Unit 1 power plant [21]. All of the structures shown in Fig. 1, the core support columns, the control rod housings in the upper plenum, the thermal shield and other miscellaneous structures are modeled. It is assumed that the fuel rods shattered upon being quenched, converting the reactor core into a large particle bed.

Spatially uniform initial conditions were chosen to simplify the interpretation of the results: in a complete accident calculation, the initial state of the debris is provided by the CORE module. In the debris bed, an initially uniform porosity of 0.4 and initial UO_2, ZrO_2 and Zr volume fractions of 0.36, 0.12 and 0.12, respectively, are prescribed. It is assumed that the Ag-In-Cd control rods melted and flowed out of the core earlier in the accident sequence. The initial pressure is 1.63×10^7 Pa and the pressure at the outlet stays fixed at this value. No water flows into the vessel during this calculation; that is, the velocity is set equal to zero at the inlet. The initial temperature of the core and the upper plenum is 645 K, which is slightly higher than the water saturation temperature at 1.63×10^7 Pa, and the region below the core is initially filled with saturated water.

The peak temperature in the core debris bed is plotted as a function of time in Fig.2. The hottest point in the bed is along the centerline and is located about 2.5 m above the lower core plate. For the first 1700 s the peak temperature in the bed increases at a constant rate of 0.5 K/s. During this time the peak temperature is less than 1500 K, oxidation is unimportant and temperatures in the bed are fairly uniform (consequently, the $\nabla^2 T$ term in Eq.(8) is small). Because the solid has not started melting, the convective terms in Eq.(8) equal zero. Neglecting energy transfer to the gas in Eq. (8) (which is a reasonable assumption only when the gas velocities are low) yields

$$\sum_j Y_{sj} \rho_{sj} c_{pj} \frac{\partial T}{\partial t} = Q\, Y_{s1} \rho_{s1} \quad . \tag{12}$$

Using the properties given in Refs.[15,16], setting Q=300 W/kg of UO_2, Y_{s1}=0.6, Y_{s2}=0.2, and Y_{s3}=0.2, gives $\partial T/\partial t$=0.55 K/s. Equation (12) gives a heating rate higher than the 0.5 K/s value calculated by the code primarily because Eq.(12) does not account for the energy required to heat the vapor.

Prater and Courtright [18] note that the Zr oxidation rate increases exponentially with temperature. When the temperature surpasses 1500 K ($t \simeq 1700$ s) the energy released by oxidation is greater than the decay heat. Between 1700 s and 2200 s the temperature increases by as much as 2.2 K/s (see Fig. 2). Zirconium starts melting and flowing downward at 2100 s. The

melt freezes upon reaching lower, colder portions of the bed, forming a dense solid crust. In the upper portion of the bed, oxidation ceases at 2300 s and the temperature increases slowly after this time.

Centerline vapor temperatures at 2000 s are shown in Fig. 3. At this time the water level is less 2 m. The oxidation rates are large and a steep axial temperature gradient has developed in the bed. Species profiles at this time are shown in Fig. 4. Note from Figs. 3 and 4 that the greatest amount of Zr is oxidized in the regions of highest temperature.

Vapor temperatures above the core region increase rapidly during the calculation, reaching 1500 K by 2000 s (see Fig.3). This is due to gas convection upward and radiation from the top of the bed. The upper core plate melts completely at 2320 s. Because stainless steel does not wet UO_2 [22], it is assumed in this study that the molten steel does not penetrate into the debris bed. Reactor Molten Pool (MP) experiments conducted at Sandia National Laboratories support this assumption: in the MP-3S experiments, UO_2 particles were placed on top of a stainless steel block and the temperature was increased until the steel melted [12]. Post-test examinations revealed that surface tension forces are large enough to support the debris bed -- that is, the particles did not sink into the debris. Experiments are needed to ascertain if the presence of Zr in the bed alters this behavior.

Porosity profiles in the bed at 2400 s are shown in Fig. 5. As discussed earlier, the molten steel rests on top of the bed. Note that a solid Zr blockage (or crust) forms about 4 m above the vessel bottom. This blockage restricts the upward flow of steam and consequently, oxidation virtually ceases in the region above the blockage. However, Zirconium still oxidizes below the blockage and the temperature in this region continues to increase rapidly. When the crust eventually melts, the Zr flows downward and refreezes closer to the bottom boundary.

4. CONCLUSIONS

Models are being implemented in the MELPROG computer code to analyze the late core melt progression phase of severe reactor accidents. A debris meltdown model has been developed and is being used to investigate oxidation, melting and refreezing in

severely damaged reactor cores. After further testing, models discussed in this study will be used to analyze the Three-Mile Island accident.

REFERENCES

1. W.J. Camp, M.F. Young, J.L. Tomkins, J.E. Kelly, P.J. Maudlin and R.J. Henninger, MELPROG-PWR/MODO: A Mechanistic Code for Analysis of Reactor Core Melt Progression and Vessel Attack under Severe Accident Conditions, NUREG/CR-4909, SAND85-0237, Sandia National Laboratories, Albuquerque, NM (1987).

2. E.L. Tolman, J.P. Adams, J.L. Anderson, P. Kuan, R.K. McCardell and J.M. Broughton, TMI-2 Accident Scenario Update, EGG-TMI-7489, Idaho National Engineering Laboratory, Idaho Falls, ID (1986).

3. S.S. Dosanjh, On the Relocation of Metallic Constituents in Core Debris Beds, NUREG/CR-5109, SAND88-0535, Sandia National Laboratories, Albuquerque, NM (1988).

4. S.S. Dosanjh and R.O. Gauntt, "MELPROG Debris Meltdown Model and Validation Experiments," 25th National Heat Transfer Conference, Houston, Tx (July 1988).

5. A.E. Scheidegger, The Physics of Flow Through Porous Media, Third Edition (Toronto and Buffalo: University of Toronto Press, 1974) pp. 266-290.

6. C.A. Wert and R.M. Thomson, Physics of Solids, Second Edition (New York, New York: McGraw-Hill Book Co., 1970) pp. 71-72.

7. A.W. Reed, K.R. Boldt, E.D. Gorham-Bergeron, R.J. Lipinski and T.R. Schmidt, DCC-1/DCC-2 Degraded Core Coolability Analysis, NUREG/CR-4390, SAND85-1967, Sandia National Laboratories, Albuquerque, NM (1985).

8. M.C. Leverett, "Capillary Behavior in Porous Solids," Pet. Trans. AIME 142, pp.152-169 (1941).

9. G.G. Brown and Associates, Unit Operations, Sixth Edition (New York, New York: John Wiley and Sons, Inc., 1956) pp. 210-228.

10. R.B. Bird, W.E. Stewart and E.N. Lightfoot, Transport Phenomena (New York, New York: John Wiley and Sons, Inc., 1960) p. 199.

11. G. Hofmann and L. Barleon, "Reduced Coolability of Particle Beds as a Result of Capillary Effects at Horizontal Phase Boundaries," Proceedings of the International ANS/ENS Topical Meeting on Thermal Reactor Safety, San Diego, California, February 2-6, 1986.

12. J.T. Hitchcock and J.E. Kelly, "Post-Test Examinations of the In-Pile Molten Pool Experiments," Trans. Am. Nucl. Soc. 43, p. 515 (1982).

13. C.P. Fryer and J.T. Hitchcock, The Postirradiation Examination of the DC Melt Dynamics Experiments, NUREG-CR-4625, SAND86-1102, Sandia National Laboratories, Albuquerque, NM (1987).

14. J.E. Kelly, J.T. Hitchcock and M.L. Schwarz, "Heat Transfer Characteristics of Dry Porous Particulate Beds with Internal Heat Generation," ASME-JSME Thermal Engineering Joint Conference Proceedings, Honolulu, Hawaii (March 1983).

15. D.L. Hagrman, G.A. Reymann and R.E. Mason, MATPRO-Version 11 (Revision 2): A Handbook of Material Properties for Use in the Analysis of Light Water Reactor Fuel Rod Behavior, NUREG/CR-0479, Idaho National Engineering Laboratory, Idaho Falls, ID (1981).

16. D.L. Hagrman, Material Property Models for Severe Core Damage Analysis, EGG-CDD-5801, Idaho National Laboratory, Idaho Falls, ID (1982).

17. Reactor Safety Research Semiannual Report January-June 1987 Volume 37, pp. 275-280, NUREG/CR-5039 (1 of 2), SAND87-2411 (1 of 2), Sandia National Laboratories, Albuquerque, NM (1988).

18. J.T. Prater and E.L. Courtright, High-Temperature Oxidation of Zircaloy-4 in Steam and Steam-Hydrogen Environments, NUREG/CR-4476, PNL-5558, Pacific Northwest Laboratory, Richland, Wa. (1986).

19. J.H. Mahaffy, "A Stability-Enhancing Two-Step Method for Fluid Flow Calculations," J. of Computaional Physics 46 (1982).

20. J.F. Harvey, Pressure Component Construction, Van Nostrand Reinhold (1980).

21. Surry Power Station Final Safety Analysis Report (FSAR), Virginia Electric and Power Company (VEPCO) (Dec. 1969).

22. R.W. Ostensen, W.F. Murphy, B.J. Wrona, L.W. Deitrich and J.C. Florek, "Intrusion of Molten Steel into Cracks in Solid Fuel in a Transient-Undercooling Accident in a Liquid-Metal Fast Breeder Reactor," Nuclear Technology 36, pp. 200-214 (1977).

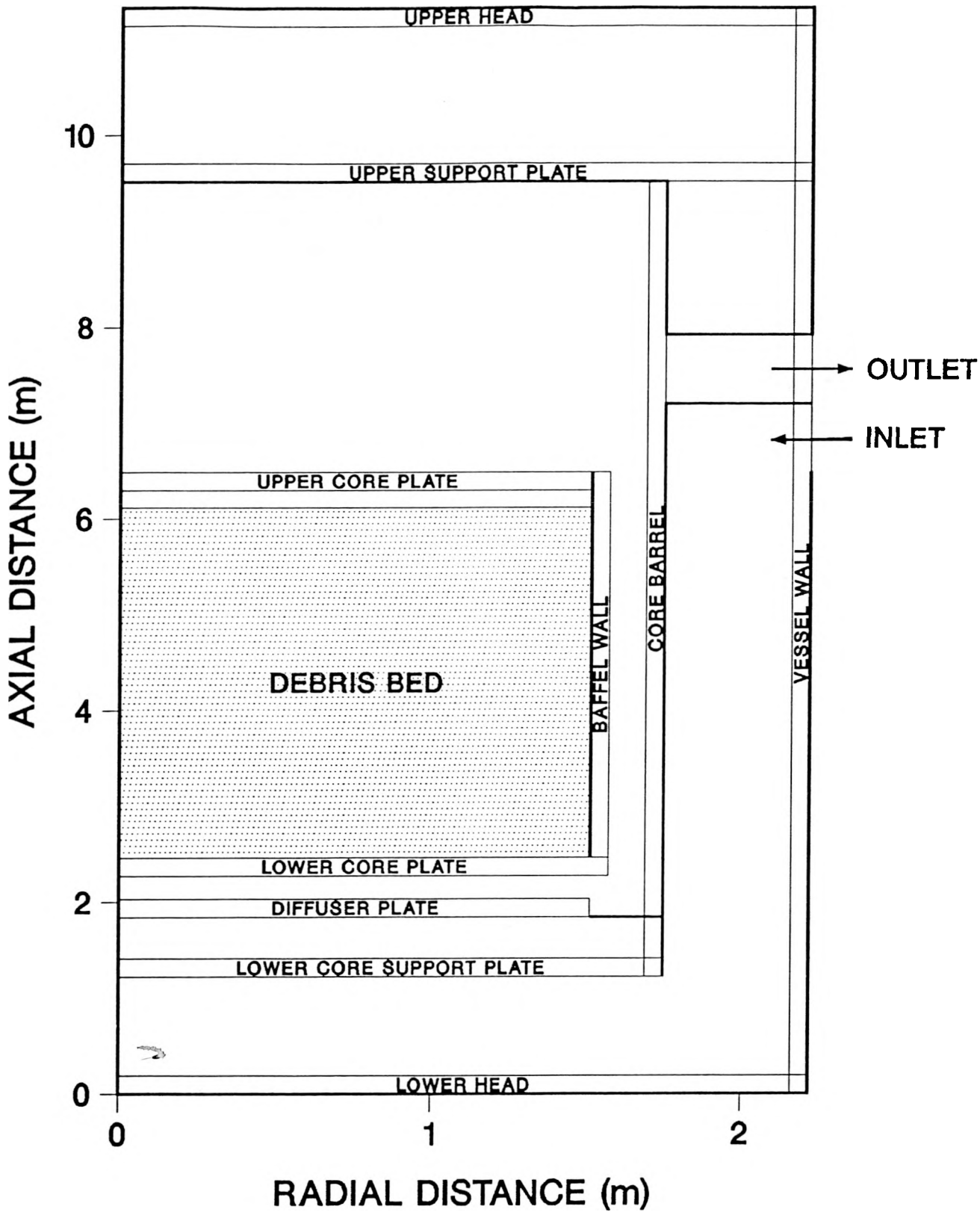

FIG. 1: Vessel model used in the demonstration calculation. Core support columns, control rod guide tubes in the upper plenum and other miscellaneous structures are not shown.

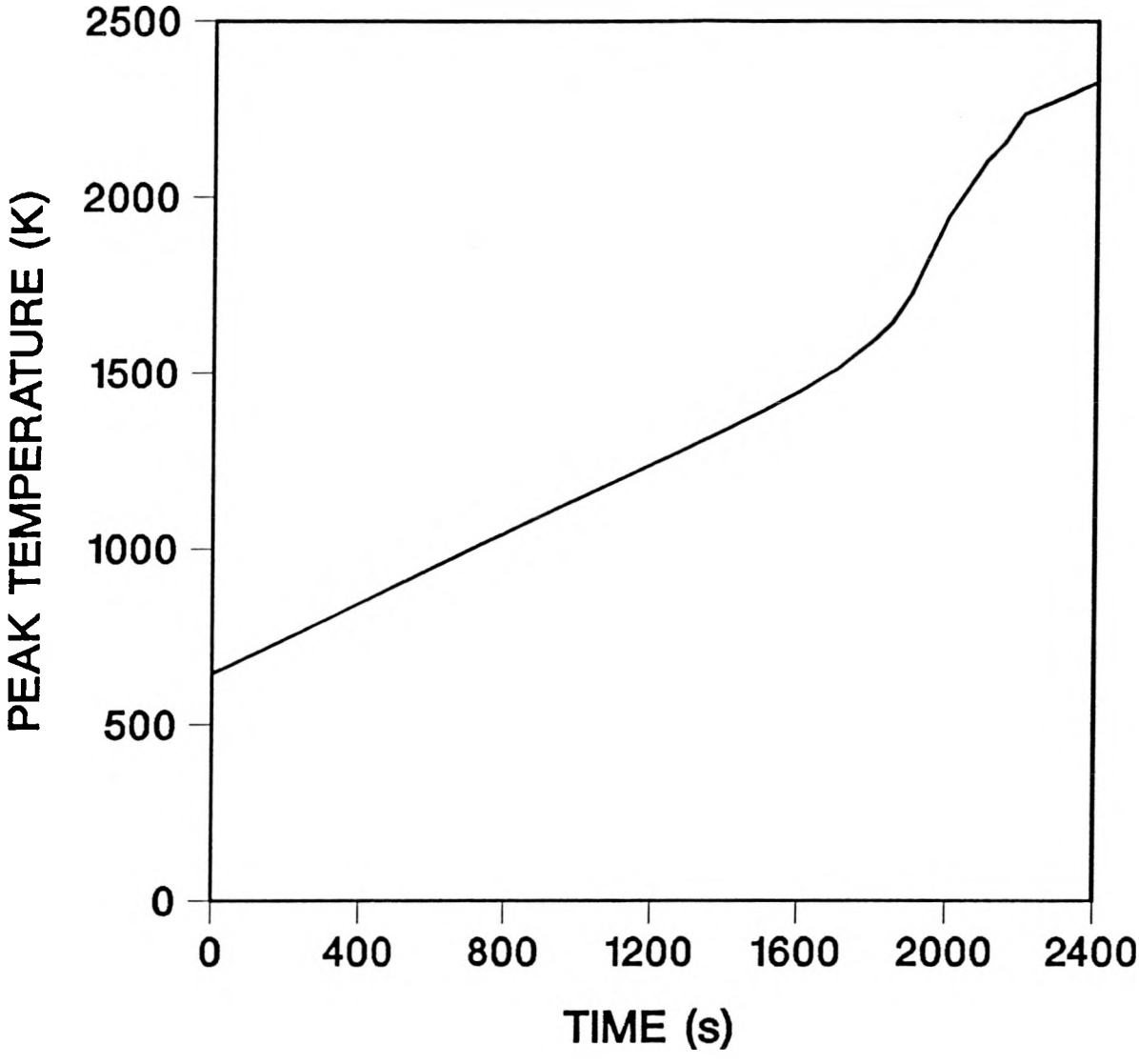

FIG. 2: Peak temperature in the debris bed as a function of time.

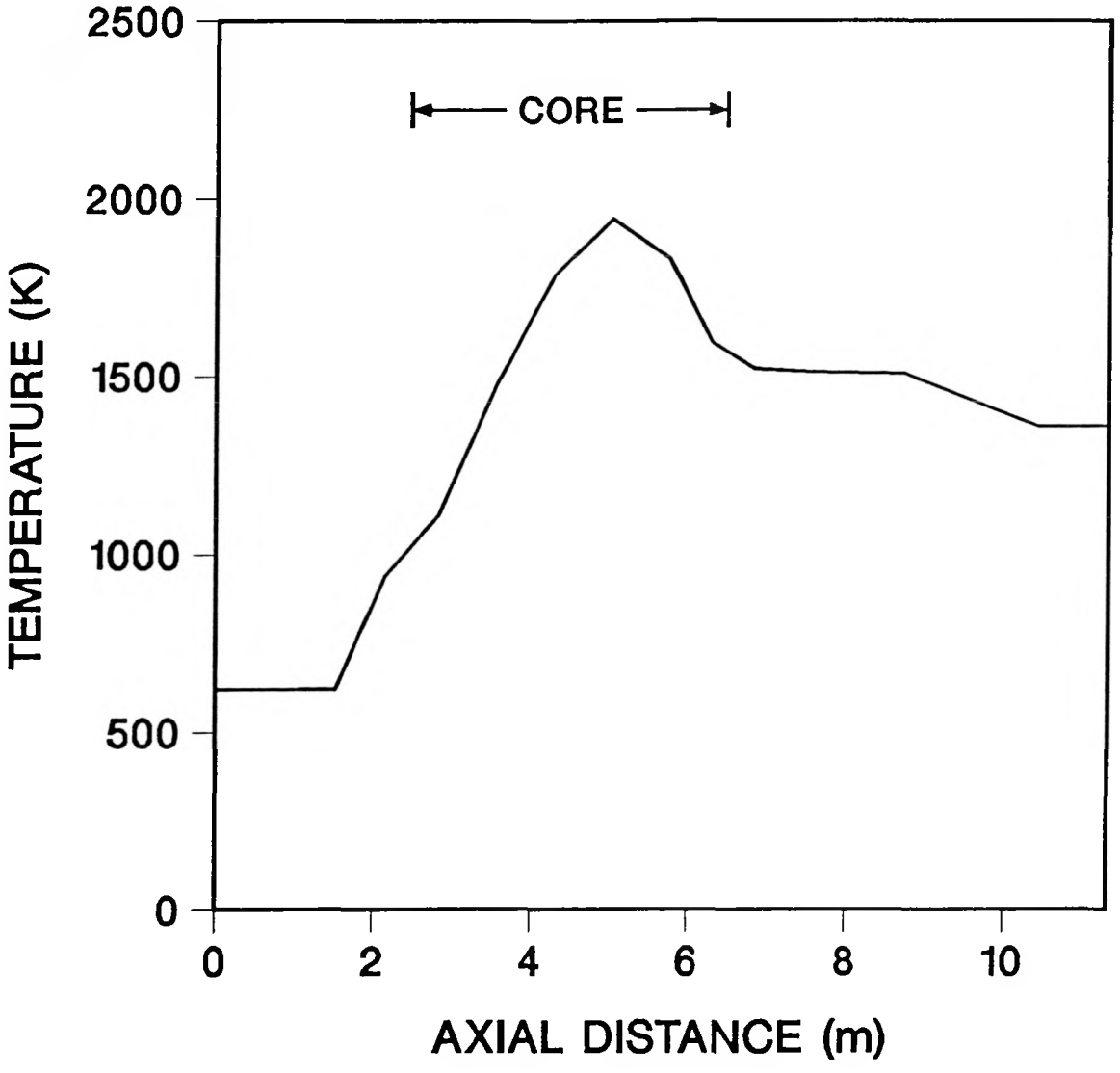

FIG. 3: Centerline vapor temperature in the vessel as a function of axial position at t=2000 s.

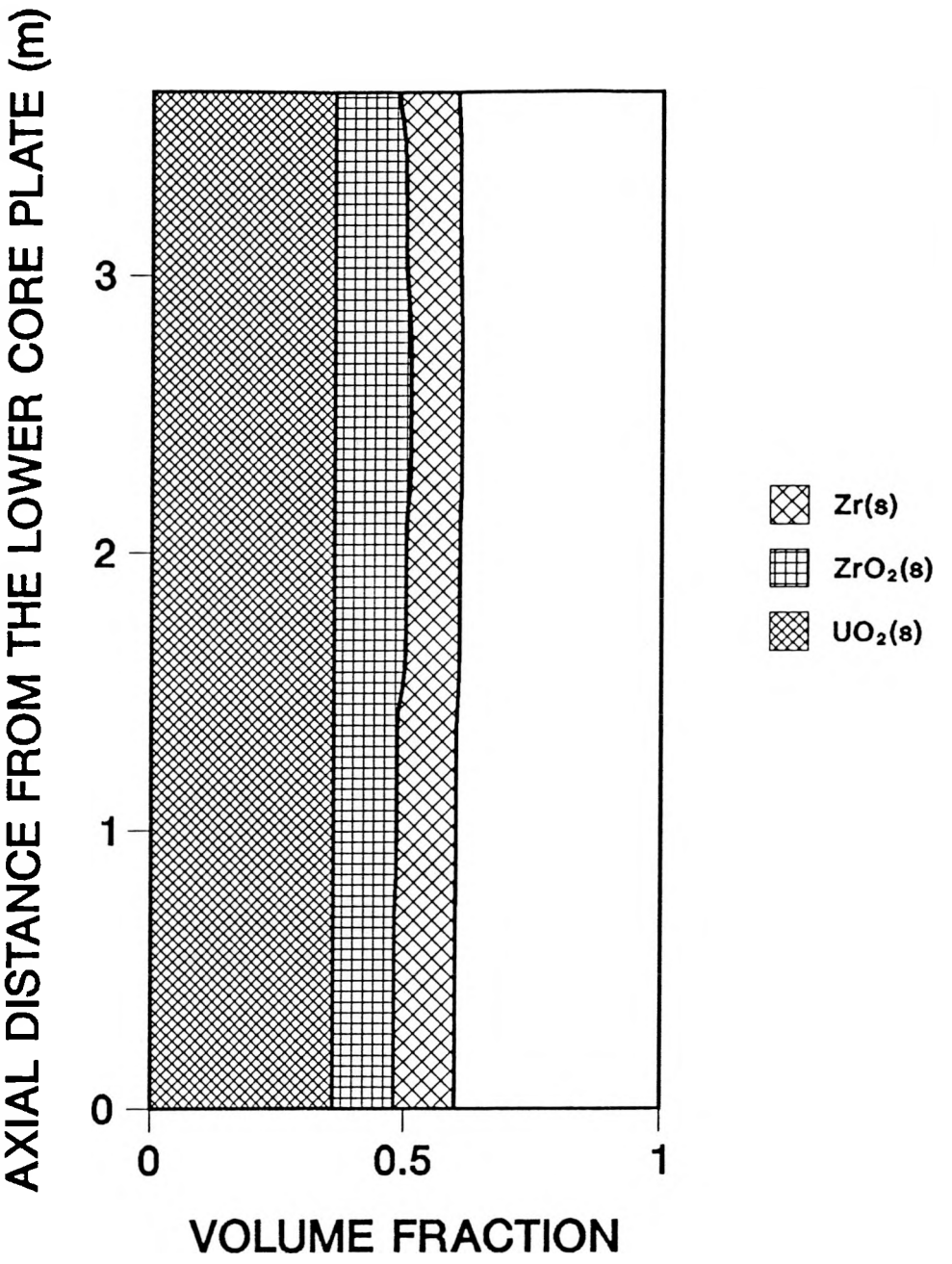

FIG. 4: Centerline species volume fractions at t=2000 s. Initially, the Zr and ZrO_2 volume fractions are equal.

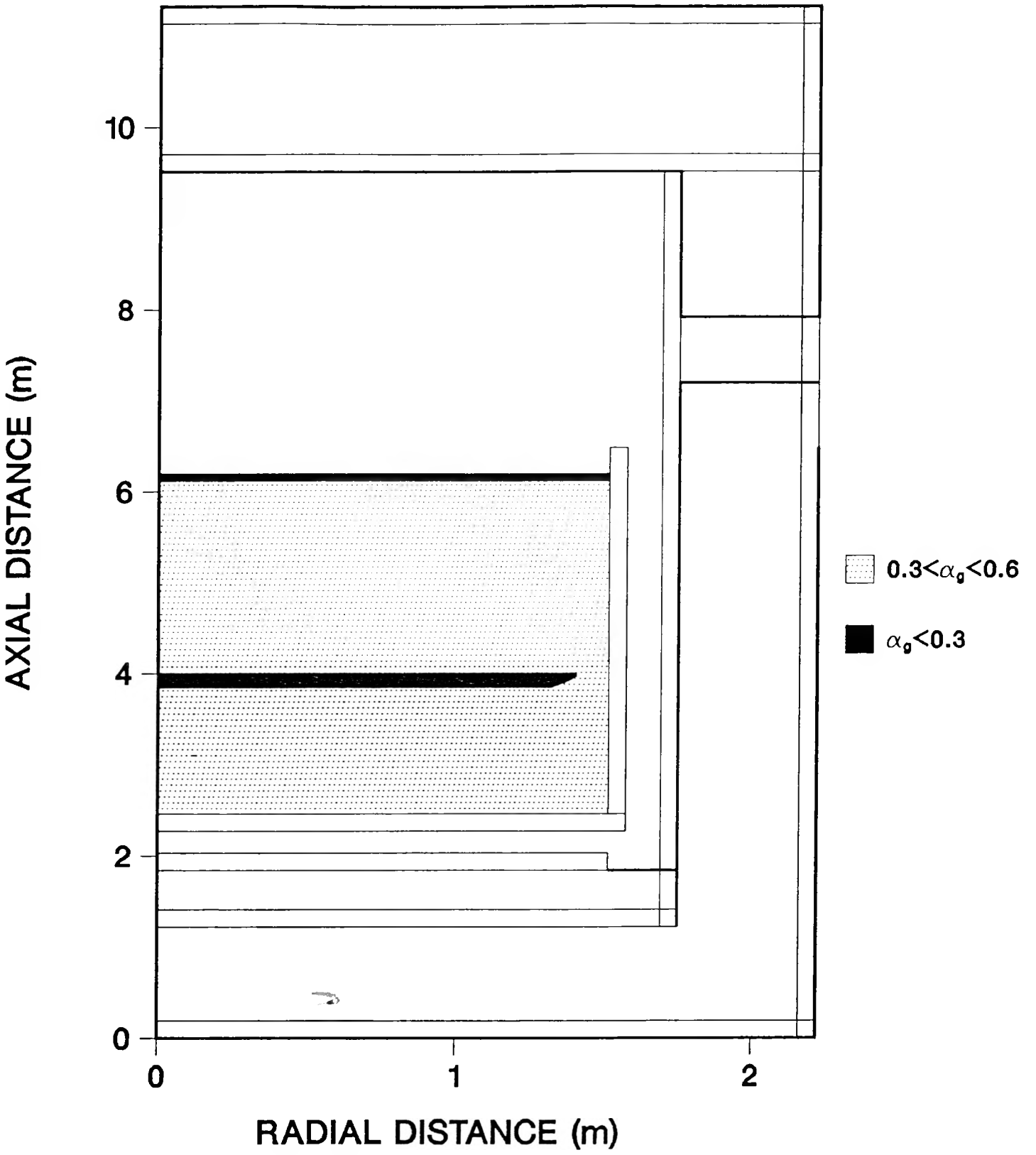

FIG. 5: Porosity α_g in the core at 2400 s.